Supporting Information

Coordination of Copper within a Crystalline Carbon Nitride and its Catalytic Reduction of CO_2

Magnus Pauly,[1] Ethan White,[1] Mawuli Deegbey,[1] Emmanuel Adu Fosu,[1] Landon Keller,[2] Scott McGuigan,[1] Golnaz Dianat,[2] Eric Gabilondo,[1] Jian Cheng Wong,[3,4] Corban G.E. Murphey,[3] Bo Shang,[5] Hailiang Wang,[5] James F. Cahoon,[3] Renato Sampaio,[3] Yosuke Kanai,[3,4] Gregory Parsons,[2] Elena Jakubikova,[1] and Paul A. Maggard[1,*]

[1] North Carolina State University, Department of Chemistry, Raleigh, NC 27695
[2] North Carolina State University, Department of Chemical Engineering, Raleigh, NC 27695
[3] University of North Carolina-Chapel Hill, Department of Chemistry, Chapel Hill, NC 27599
[4] University of North Carolina-Chapel Hill, Departments of Physics and Astronomy, Chapel Hill, NC 27599
[5] Yale University, Department of Chemistry, New Haven, CT 06520

Structural Characterization. Powder X-ray diffraction (PXRD) data on the PTI/Cu materials were taken using Mo Kα radiation (λ = 7093 Å) from a sealed tube X-ray source (40 kV, 36 mA). The crystalline structures of 1-PTI/LiCuCl, 2-PTI/Cu_2Cl and 3-PTI/HCuCl were characterized on samples that had been reacted with excess CuCl (1 and 2) and $CuCl_2$ (3), respectively, to yield the maximal amounts of Cu within their carbon nitride layers, as judged by elemental analysis. The structures were refined within the software package GSAS-II.[2] The crystal structure of 1-PTI/LiCuCl was consistent with that reported previously[1] in the space group of C*mc2₁* and gave refined lattice parameters of *a* = 14.727(5) Å, *b* = 8.515(3) Å, and *c* = 6.7343(4) Å with a unit cell volume of 844.5(1) Å^3. The crystal structure of 2-PTI/Cu_2Cl could be best fitted to a similarly constructed PTI structure from the previously published structural model[1] in the space group P*2₁/m* and refined lattice parameters *a* = 8.509(3) Å, *b* = 6.7278(2) Å, *c* = 14.721(6) Å, and *β* = 90.23(4)°. By contrast, the PXRD data of 3-PTI/HCuCl could not be refined against any known structures as reported for several ordered or disordered experimental polymorphs for PTI/LiCl,[1,3,4] PTI/HCl,[5] or theoretical polymorphs with different amounts and configurations of Cu/Li/H atoms within the intralayer cavities.[1,6] In each case, least squares refinements of the models could not be fitted to a significant fraction of the diffraction peaks nor yielded a weighted residual less than ~20-30%.

Analysis of the PXRD pattern for 3-PTI/HCuCl shows a significant reduction in the interlayer distance at ~3.24 Å (labeled in Figure S1) as compared to the usual interlayer

distance for PTI/LiCl, 1-PTI/LiCuCl, and 2-PTI/Cu_2Cl of ~3.4 Å. Difference Fourier maps of the electron density revealed a disordered arrangement of the chloride anion over two separate positions. As the chloride anion is observed in known structural models to be located either within the planes of the bridged triazine rings, or occurring between them, this suggested the possibility of two different layers. Thus, refinements of structural models were attempted consisting of two types of layers, converging on a two-phase model consisting of layers of PTI/HCl and PTI/Cu_2Cl. The refinement began with fitting the background (25 coefficients) and refinement of the initial structural model as found experimentally for PTI/Cu-low in space group C*mc2*$_1$ with *a* = 14.755(4) Å, *b* = 8.557(3) Å, and *c* = 6.4193(6) Å and a unit cell volume of 810.5(2) Å^3. At this stage, a large fraction of the diffraction peaks (~25%) could not be accounted for by the model. Next, the residual electron density was modeled by the incorporation of the reported structure of PTI/HCl, centered around the position of the second site of the disordered chloride anion.[4,5] The refined structural model yielded a weighted residual wRp of ~7.3% and accounts for the full set of experimental diffraction peaks, Figure S2. This disordered stacking model of mixed layers yields two stacking distances (~3.24 and ~2.38 Å) because of the alternating layers of PTI/CuCl and PTI/HCl. The 3.24 Å corresponds to the typical PTI layer to PTI layer distance. The shorter distance of 2.38 Å corresponds to the new PTI/Cu_2Cl to PTI/HCl stacking, in which the Cl atoms of the PTI/HCl layers coordinate to the Cu atoms of the neighboring PTI/Cu_2 layers (above and below).

Morphological, Elemental and Surface Characterization of Crystallites. Scanning electron microscopy was used to characterize particles of each Cu-coordinated compound after being electrophoretically deposited onto FTO and graphite slides at an applied bias of -1.4 V vs Ag/AgCl in an aqueous bicarbonate solution (0.5 M $KHCO_3$) for a time of 1.5 h. Top-down scanning electron microscope (SEM, FEI Verios 460L) was used as operated at 13 pA current and 0.5 to 2 kV electron landing energy with sample bias of 0 to 0.5 kV. EDS data were collected to analyze elemental compositions of samples. X-ray photoelectron spectroscopy was also used to probe the elemental distribution and copper oxidation state in the 1-PTI/LiCuCl and 3-PTI/HCuCl crystallites both before and after the electrophoretic deposition and electrocatalytic CO_2 reduction. The XPS instrument (XPS, Kratos Analytical Axis Ultra) was equipped and operated with an Al Kα (1486.6 eV) gun, at a power of 10 mA and 15 kV. All spectra were calibrated by shifting the adventitious C 1s peak to 248.8 eV. The survey spectra and high-resolution scans for C 1s, N 1s, Cu 2p, Cu LMM regions were acquired for each sample.

Electrocatalytic CO_2 Reduction: A quartz H-cell was utilized that consisted of two ~10 ml cells connected by a bipolar membrane. The reduction cell contained ~14 ml of buffered solution with the suspended, powdered PTI/Cu catalyst. The head space was sealed by a compression top with four ports, a gas inlet (fritted), gas outlet, sampling septa, and a glassy carbon electrode. The oxidation cell is fitted with a platinum wire counter electrode and Ag/AgCl reference electrode. The buffer solution was 0.5 M potassium bicarbonate ($KHCO_3$) at pH ~ 6.8.The PTI/Cu powders (~40 micromoles) were kept suspended via stirring with a magnetic stir bar. Samples were purged with CO_2 then an applied bias was swept from 0 to -1.7 V. A constant applied bias was also tested at -0.7 V, -1.4 V, and -1.7 V for ~20 h to identify the optimal film formation and its response and stability. The applied bias of -1.4 V yielded the best balance of cathodic

current for CO_2R and film stability. To establish trends between materials, these measurements were repeated ~3 times each for g-CN, PTI/LiCl, 1-PTI/LiCuCl and 3-PTI/HCuCl. The films were deposited by applying a constant bias for several hours (varying from ~2 h to ~22 h). The 1-PTI/LiCuCl and 3-PTI/HCuCl exhibited a steady increase in cathodic current with time e.g., shown in Figure S4, after which the film was placed in a fresh solution and the currents remained stable for the remainder of the CO_2R experiments. Liquid products were analyzed by proton nuclear magnetic resonance spectroscopy (^{1}H NMR) and gaseous products were analyzed by gas chromatography with thermal conductivity detector (GC-TCD).

Computational Methodologies. As the starting point of GW calculations[7,8], density functional theory (DFT) calculations were performed using Quantum ESPRESSO code.[9] The Kohn-Sham (KS) wave functions were represented in a plane-wave basis using the norm-conserving ONCV pseudopotentials[10,11] with a kinetic energy cutoff of 50 Ryd. PBE0[12] hybrid exchange-correlation approximation[13] was used in the calculations. Using the KS orbital and energies, quasiparticle (QP) energies were obtained by performing GW method calculation within the G_0W_0 approximation using BerkeleyGW code.[14] Hybertsen-Louie generalized plasmon pole model[7] was used to model the dielectric function and random phase approximation was used for the screened Coulomb interaction. The GW calculations were converged to within 1 k_BT with respect to parameters. An 80-atom supercell with periodic boundary conditions (PBC) was used for the calculation of the bulk PTI system. The dimension of the supercell used was 14.67 Å x 8.47 Å x 6.72 Å, and it consists of two layers of PTI in the A1a structure.[1] Each layer contains two pores with the cation located in-plane within the PTI layer while the halides are intercalated in between the pores of the two PTI layers. A 2 x 4 x 4 Monkhorst-Pack k-point grid[15] was used for sampling the Brillouin zone. The two-dimensional monolayer of PTI was modeled using a 36-atom supercell, and its dimension was 14.67 Å x 8.47 Å x 20.00 Å. One cation atom was removed from each pore of the PTI to ensure that the system remained charge neutral. While 2-PTI/Cu_2Cl and 3-PTI/HCuCl showed two Cu cations per pore, the use of PBC in the calculation makes it difficult to model this kind of charge non-neutral situation. The calculations were performed using a 2 x 4 x 1 k-point grid sampling the Brillouin zone.

For calculation of the mechanistic pathway of CO_2 reduction, DFT methods utilizing the B3LYP functional[16] was employed for optimization of all complexes in this study. Note that a molecular model of a single pore was employed in these calculations (see Figure S10) as that allows us to easily account for the solvent effects as well as the charge changes at the catalytic center due to the reduction events and proton transfers. Additionally, we have confirmed that the basic electronic structure of the molecular model is in a good agreement with the electronic structure of the monolayer, with the frontier orbitals (HOMO and LUMO) being localized on the two Cu atoms (see Figure S11). The 6-311G* basis set was used for all atoms (H, C, N, O),[17,18] except for Cu, where the Stuttgart-Dresden (SDD) basis sets and its accompanying pseudopotential was employed.[19] Solvent effects (water) were included in all the calculations via the polarizable continuum model (PCM).[20] Vibrational frequency analysis was performed to

ensure that the optimized structures correspond to minima on their respective potential energy surfaces. The frequency calculations were also used to obtain zero-point energies and entropic corrections to the free energy (assuming a temperature of 298.15 K and 1.0 atm, respectively) using standard statistical mechanical conventions. The calculated reduction potentials (E°) were determined relative to the ferrocene couple through equation 1:

$$E°(in\ V) = \ -\frac{\Delta Gsol}{nF} - 5.25 \qquad (1)$$

where *ΔGsol* is the change in solvated free energy upon reduction, *n* is the number of electrons (in this case, 1), and *F* is the Faraday constant. The calculated half-cell potential for the ferrocene couple (5.25 V) was obtained by using the same level of theory as that of the complexes since this reduces the errors in the calculated redox potential.[21] In order to report the redox potential vs Ag/AgCl, a 0.45 V correction factor was added. All calculations were carried out using the Gaussian 16, Revision A.03 software package.[22]

Table S1. Rietveld refinements of Cu-substituted PTI/LiCl models according to the space group, and additional identifiers as needed. Best fits are highlighted in red.

			2-PTI/Cu_2Cl		3-PTI/HCuCl	
Model	**Ref.**	**Space Group**	**wR%**	**Extra peaks**	**wR%**	**Extra peaks**
Liao	23	C*mc2*$_1$	9.675	-2	17.488	0
Wirnhier	3	P*6*$_3$*cm*	9.808	-2	27.278	1
Mesch	4	P*2*$_1$*2*$_1$*2*$_1$	10.212	-2	15.139	3
Pauly-A1	1	A*ma2*	10.295	-2	15.875	0
Pauly-A2	1	C*mcm*	11.196	-2	19.551	0
Pauly-B1	1	P*bcm*	7.74	1	17.763	1
Pauly-B2	1	P*nma*	6.236	2	17.756	2
Pauly-C1	1	P*2*$_1$*/m*	6.796	1	15.99	0
Pauly-C2	1	P*2*$_1$*/m*	6.028	0	18.235	3
Multilayered model		C*mc2*$_1$			7.716	0

Table S2. Elemental composition of each form of PTI/Cu compared to PTI/LiCl. Black values were measured by FAA, red values by ICP-MS, and blue by EDS.

Material	**Li**	**C**	**N**	**Cu**	**H**
PTI/LiCl	2.01	6.00	9.16	0	3.15
1-PTI/LiCuCl	0.89	6.10	9.00	1.09	2.32
2-PTI/Cu_2Cl		6.23	9.00	1.99	
3-PTI/HCuCl	0.18	6.23	9.00	1.06	3.79

Table S3. Elemental composition from XPS analyses of survey spectra. Values are given in atomic percentages.

	Elemental Atomic Percentages (± 1%)								
Sample	C 1*s*	O 1*s*[a]	N 1*s*	Cu 2*p*	Cl 2*p*	Li 1*s*	Na 1*s*[a]	Si 2*p*[a]	Al 2*p*[a]
3-PTI/HCuCl (before CO_2R)	42	2	44	4	6	2	-	-	-
3-PTI/HCuCl (after CO_2R)	46	35	2	2	1	<1	7	3	4

[a] Elemental contributions as derived from the bicarbonate buffer solution (after drying) and the underlying electrode substrate.

Table S4. Table of product distribution and Faradaic Efficiencies (FE) from electrophoretic deposition of 3-PTI/HCuCl particles from a 0.5M $KHCO_3$ solution at -1.16 V versus SHE.

[a]Run #	CO FE %	H_2 FE %	Formate FE %	Gases FE %	Total CO_2 Reduction FE %	Net FE %
1	9.3	39.2	12.4	48.5	21.7	60.9
2	15.6	46.3	18.1	62.0	33.7	80.0
3	2.1	57.6	7.2	59.8	9.3	66.9
Average	9.0	47.7	12.6	56.8	21.6	69.3

[a] PTI/Cu particles were electrophoretically deposited at -1.16 V versus SHE in a 0.5M $KHCO_3$ aqueous solution for 90 minutes each, from the same suspension of particles. Run 1 represents the first 90 min, where the smallest particle are extracted from solution, followed by subsequent Runs 2 and 3, each for 90 min under the same conditions.

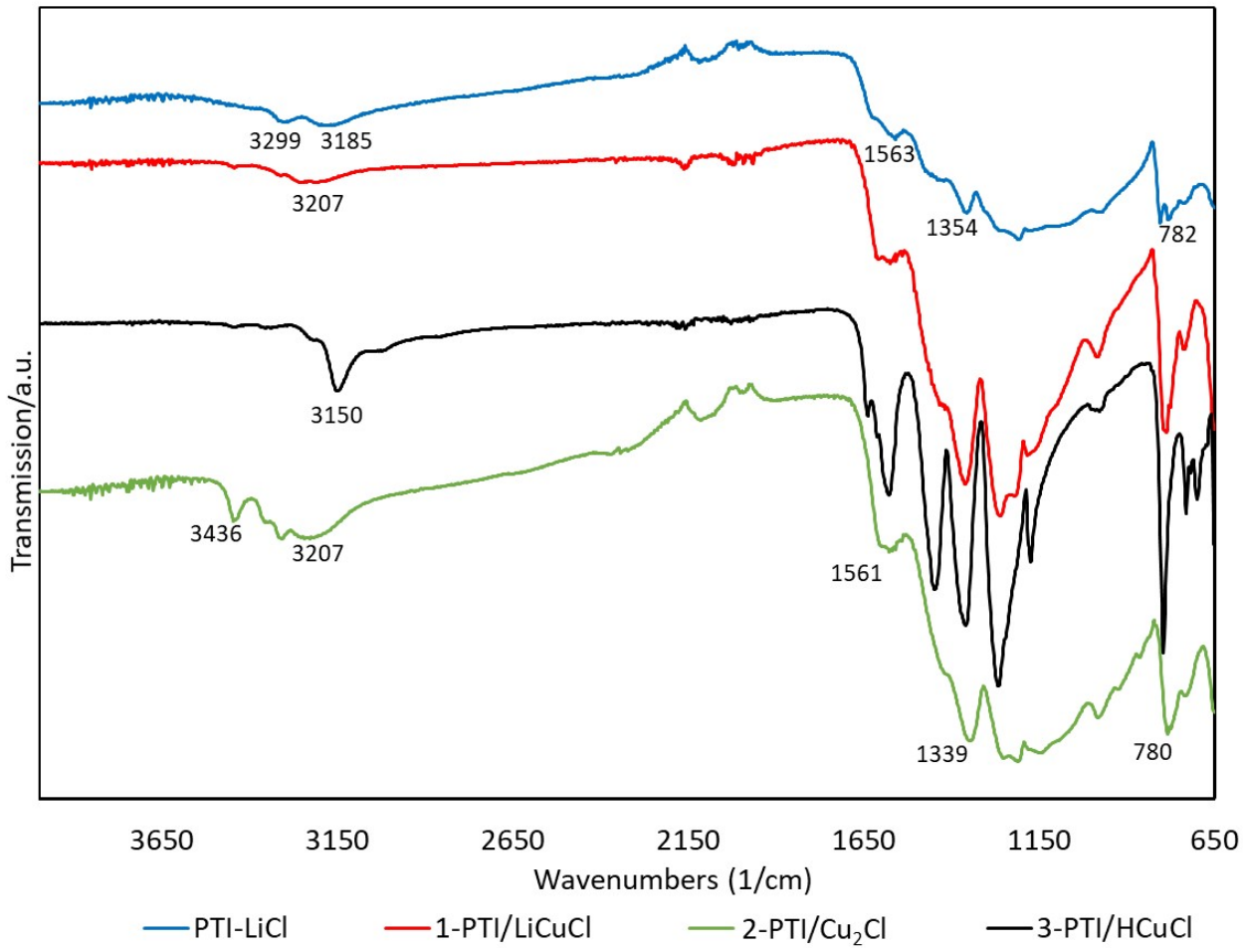

Figure S1. A comparison of the mid-range FT-IR absorbance of PTI/LiCl (blue), 1-PTI/LiCuCl (red), 2-PTICu_2Cl (black), and 3-PTI/HCuCl (green); showing the C-N stretching regions are consistent across each material, and the increase in the N-H stretching region for PTI/Cu consistent with an increased number of N-H groups.

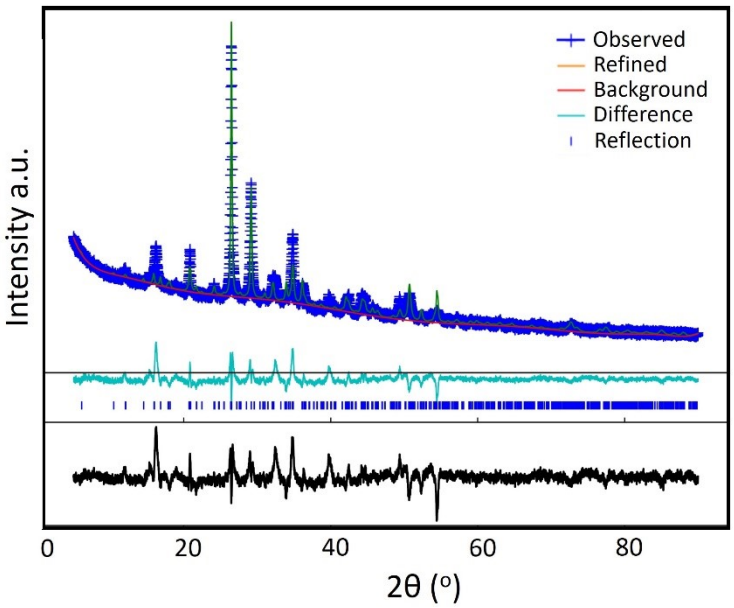

Figure S2. Plot of the Rietveld refinement of the structure of **2**-PTI/Cu_2Cl, with the labels indicated for observed data, calculated diffraction pattern, background, and difference.

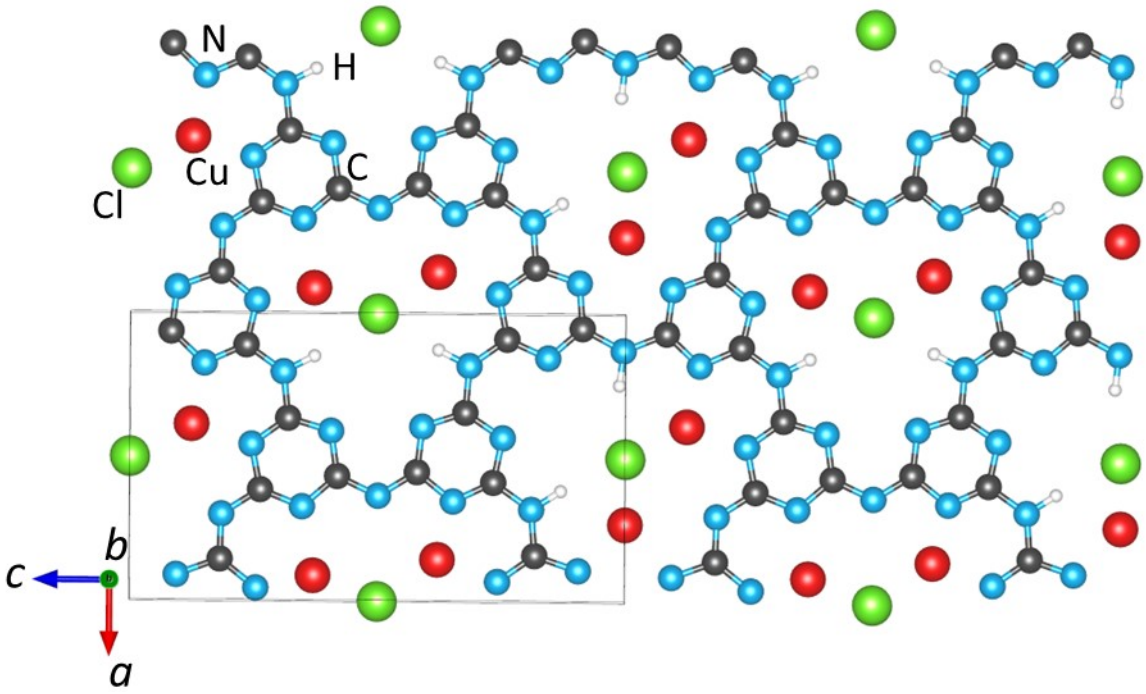

Figure S3. Refined crystal structure of **2**-PTI/Cu_2Cl, showing a single carbon-nitride layer. Nitrogen atoms are depicted as blue, carbon as black, hydrogen as white, copper as red, and chloride as green.

Table S5. Listing of refined atomic coordinates, site occupancies and isotropic displacement parameters (Å^2) for 2-PTI/Cu_2Cl with lattice parameters *a* = 8.509(3) Å, *b* = 6.7278(2) Å, *c* = 14.721(6) Å, and *β* = 90.23(4) ° in space group $P2_1/m$. Note hydrogen positions were unrefined from published model.[1]

Atom	x	y	z	Site Mult.	U_{iso}
C1	0.14552	0.75	0.1823	2e	0.0021(3)
C2	0.16223	0.75	0.81746	2e	0.0021
C3	0.65823	0.75	0.67642	2e	0.0021
C4	0.63641	0.75	0.31894	2e	0.0021
C5	0.93637	0.75	0.08211	2e	0.0021
C6	0.95258	0.75	0.91222	2e	0.0021
C7	0.45096	0.75	0.57943	2e	0.0021
C8	0.43526	0.75	0.41852	2e	0.0021
C9	0.89061	0.75	0.23373	2e	0.0021
C10	0.91373	0.75	0.76026	2e	0.0021
C11	0.41591	0.75	0.73353	2e	0.0021
C12	0.38759	0.75	0.26305	2e	0.0021
N1	0.88916	0.25	0.0944	2e	0.0021
N2	0.90966	0.25	0.90591	2e	0.0021
N3	0.40748	0.25	0.59433	2e	0.0021
N4	0.39093	0.25	0.41025	2e	0.0021
N5	0.04555	0.75	0.25475	2e	0.0021
N6	0.07122	0.75	0.7427	2e	0.0021
N7	0.5708	0.75	0.75211	2e	0.0021
N8	0.54542	0.75	0.24523	2e	0.0021
N9	0.8261	0.75	0.14928	2e	0.0021
N10	0.84936	0.75	0.84307	2e	0.0021
N11	0.34982	0.75	0.65241	2e	0.0021
N12	0.3292	0.75	0.34769	2e	0.0021
N13	0.302	0.75	0.18501	2e	0.0021
N14	0.32267	0.75	0.8106	2e	0.0021
N15	0.82125	0.75	0.68418	2e	0.0021
N16	0.79788	0.75	0.30921	2e	0.0021
N17	0.87648	0.75	0.99518	2e	0.0021
N18	0.36782	0.75	0.50109	2e	0.0021
Cu1	0.082(4)	0.75	0.373(3)	2e	0.0156(6)
Cu2	0.073(5)	0.75	0.620(3)	2e	0.0156
Cu3	0.617(4)	0.75	0.121(4)	2e	0.0156
Cu4	0.750(3)	0.25	0.031(2)	2e	0.0156
Cl1	0.5	0	0	2e	0.0156
Cl2	0	0	0.5	2e	0.0156

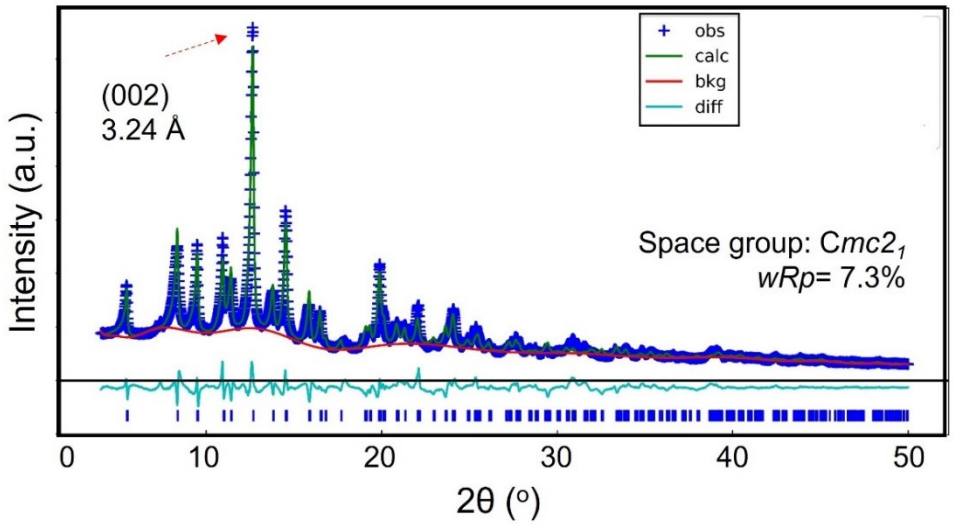

Figure S4. Plot of the Rietveld refinement of the structure of **3**-PTI/HCuCl in the space group C$mc2_1$, with the labels indicated for observed data, calculated diffraction pattern, background, and difference.

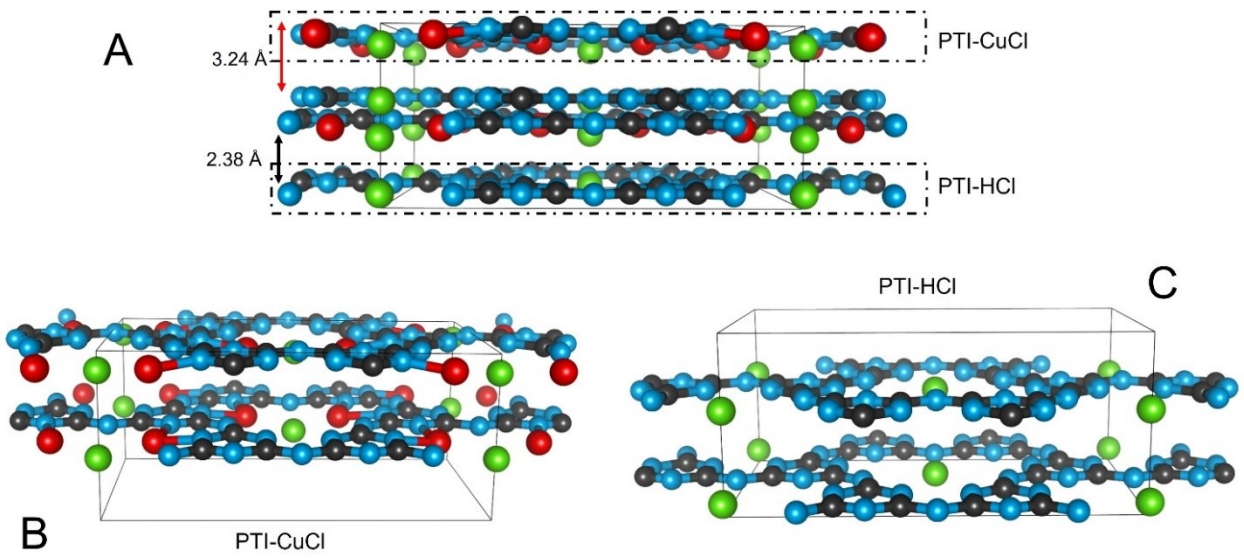

Figure S5. (A) View of the refined mixed "PTI/HCl:PTI/Cu_2Cl" layer structure of 3-PTI/HCuCl with layer-to-layer distances labeled and the two types of layers drawn individually in (B) for the PTI/Cu_2Cl layer and (C) for the PTI/HCl layer. H atoms are bonded to the N-triazine and N-imide groups but are not shown for clarity.

Table S6. Listing of refined atomic coordinates, site occupancies and isotropic displacement parameters (Å^2) for 3-PTI/HCuCl with lattice parameters *a* = 14.755(2) Å, *b* = 8.565(2) Å, and *c* = 6.4214(4) Å in space group C*mc2*$_1$. Note hydrogen positions are not assigned.

Atom	x	y	z	Occupancy	Site Mult.	Uiso
N1	0.165(1)	0.34184	0.968(3)	0.57(1)	8b	0.072(2)
N2	0.083(1)	0.5542	0.968(3)	0.57(1)	8b	0.072
N3	0.1650(4)	0.34184	0.598(2)	0.42(1)	8b	0.072
N4	0.0832(4)	0.5542	0.598(2)	0.42(1)	8b	0.072
N5	0.745(1)	0.05923	0.968(3)	0.57(1)	8b	0.072
N6	0.000(1)	0.32632	0.968(3)	0.57(1)	4a	0.072
N7	0.182(1)	0.80413	0.968(3)	0.57(1)	8b	0.072
N8	0.7450(4)	0.05923	0.598(2)	0.42(1)	8b	0.072
N9	0.0000(4)	0.32632	0.598(2)	0.42(1)	4a	0.072
N10	0.1828(4)	0.80413	0.598(2)	0.42(1)	8b	0.072
C1	0.739(1)	0.89712	0.969(3)	0.57(1)	8b	0.072
C2	0.7399(4)	0.89712	0.597(2)	0.42(1)	8b	0.072
C3	0.084(1)	0.3938	0.969(3)	0.57(1)	8b	0.072
C4	0.165(1)	0.66314	0.969(3)	0.57(1)	8b	0.072
C5	0.0845(4)	0.3938	0.597(2)	0.42(1)	8b	0.072
C6	0.1650(4)	0.66314	0.597(2)	0.42(1)	8b	0.072
Cu1	0.8680(7)	0.870(2)	0.433(2)	0.503(7)	8b	0.050
Cl1	0.000(5)	0.994(1)	0.884(3)	0.57(1)	4a	0.050(6)
Cl2	0.000(8)	0.9998(4)	0.579(2)	0.42(1)	4a	0.050

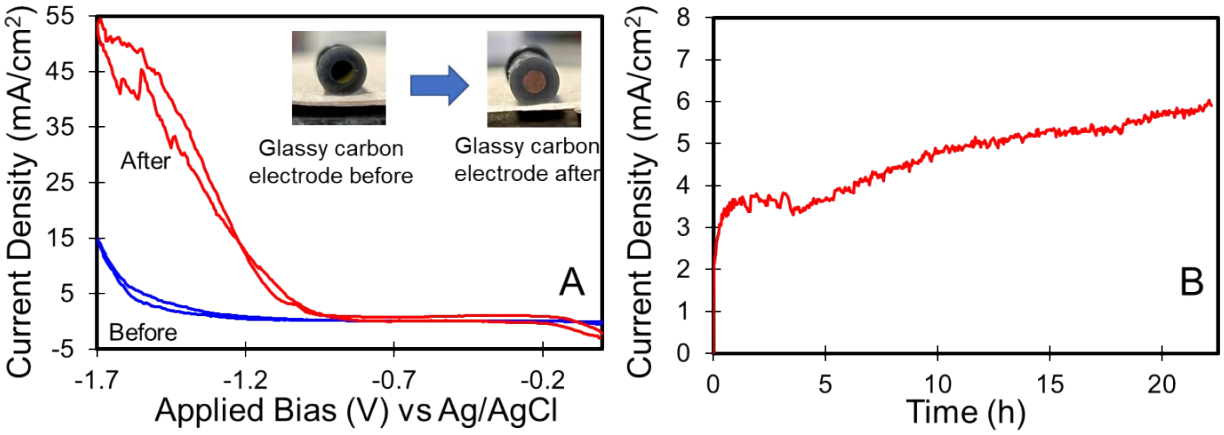

Figure S6. Left, results of cyclic voltammetry of suspended crystallites of 3-PTI/HCuCl both before and after electrophoretic deposition for 22 h in 0.5M $KHCO_3$ and right, extended chronoamperometry of 3-PTI/HCuCl suspension in a quartz single cell during the electrophoretic deposition process at -1.4 V applied bias versus Ag/AgCl.

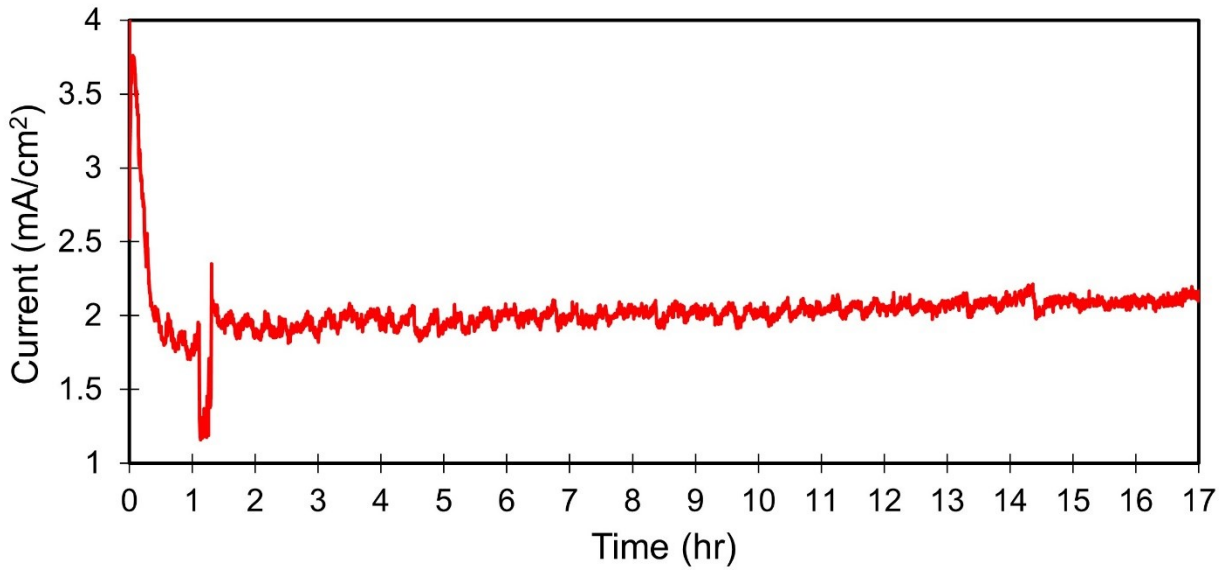

Figure S7. Results of extended chronoamperometry of electrophoretically-deposited film of 3-PTI/HCuCl in a H-Cell, with applied bias of -1.16 V versus SHE when placed in a fresh solution of 0.5M $KHCO_3$ saturated with CO_2(g) with a pH ~ 7-8.

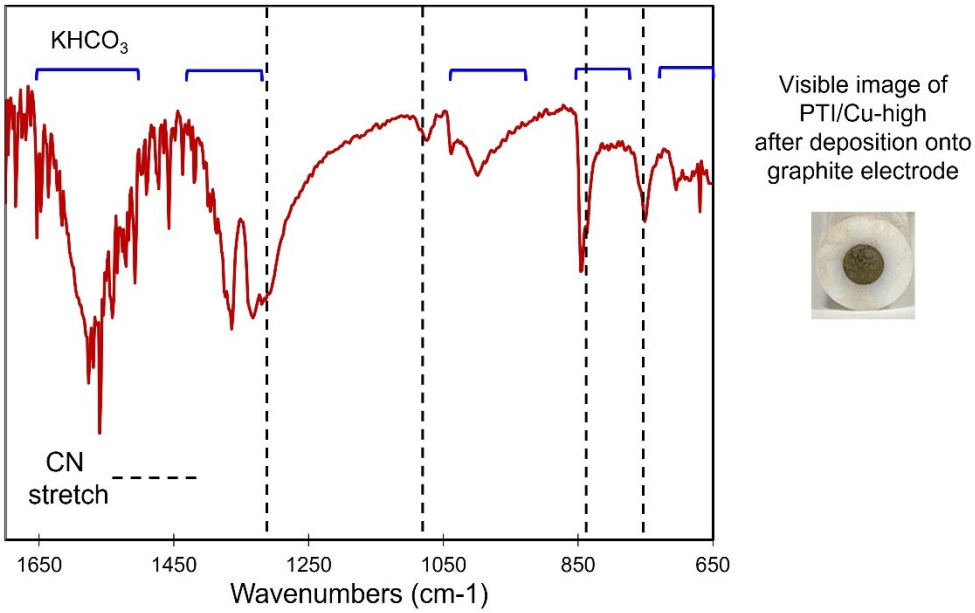

Figure S8. FT-IR absorbance of electrophoretically-deposited 3-PTI/HCuCl, with the stretching regions labeled for $KHCO_3$ (blue) and the carbon nitride framework (dashed lines).

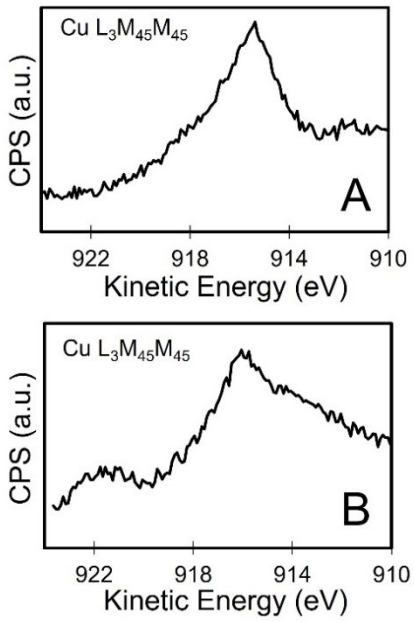

Figure S9. *Ex-situ* XPS high resolution spectra of Cu $L_3M_{45}M_{45}$ Auger region for a) 3-PTI/HCuCl powder before reaction and B) 3-PTI/HCuCl on electrode surface after CO_2R reaction.

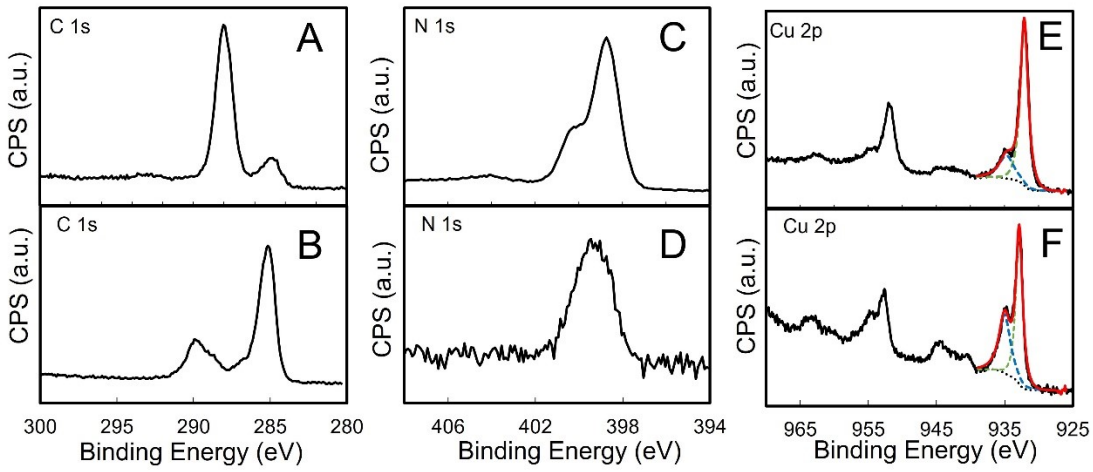

Figure S10. *Ex-situ* XPS high resolution spectra of C 1*s*, N 1*s*, and Cu 2*p* regions for 3-PTI/HCuCl powder before reaction (A, C, E; respectively) and PTI/Cu-high on electrode surface after CO_2R reaction (B, D, F; respectively).

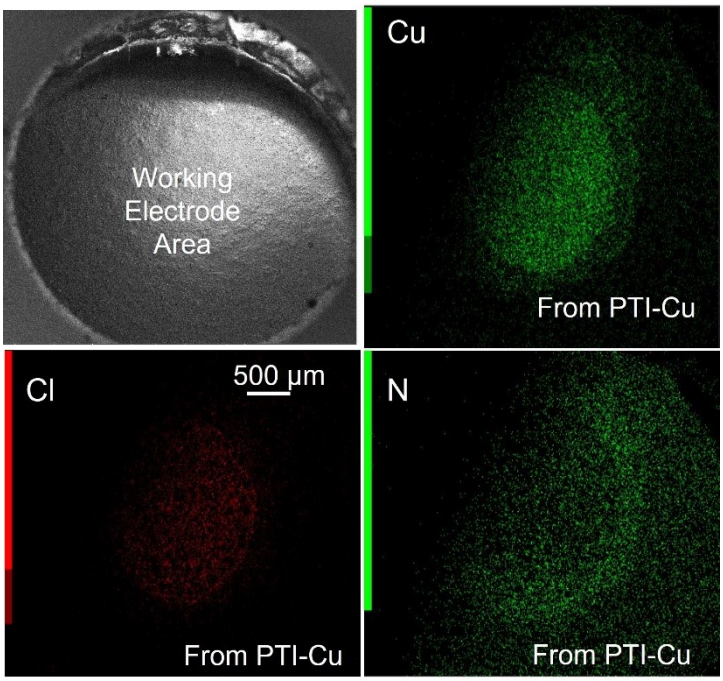

Figure S11. Scanning electron microscope image of working electrode surface (upper left) and EDS maps after electrophoretic deposition of Cu/PTI onto a graphite electrode at -1.4 V for 1.5 h. Elemental contributions for Cu, Cl and N are shown, while the C content was not determined because of the background contribution from the graphite electrode.

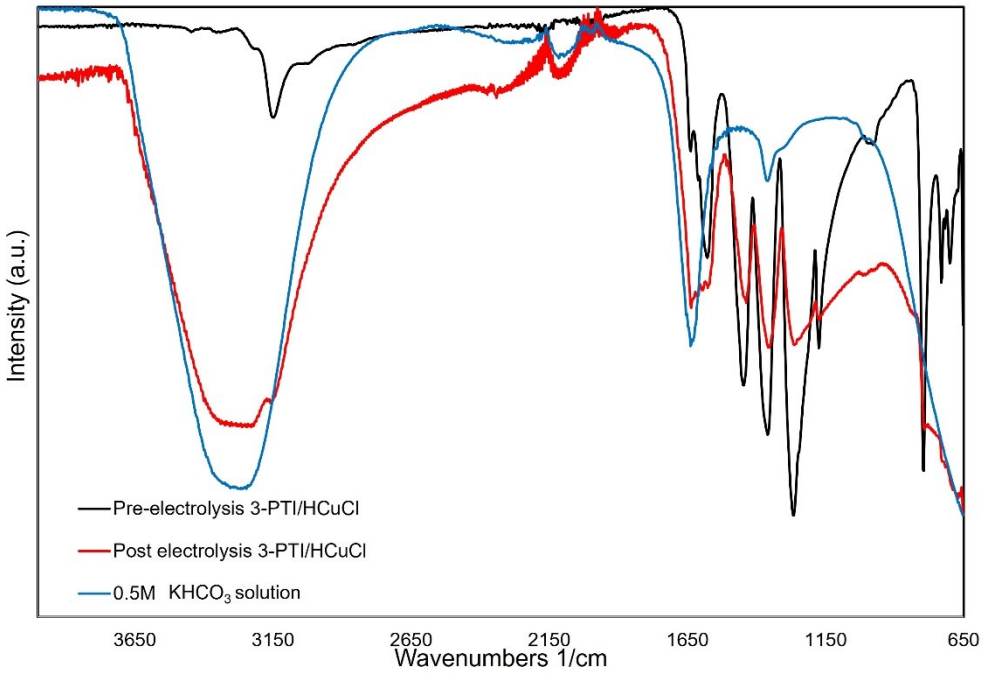

Figure S12. FT-IR absorbance of electrophoretically-deposited 3-PTI/HCuCl before before (black) and after (red) electrocatalytic CO_2 reduction, and of the 0.5 M $KHCO_3$ solution.

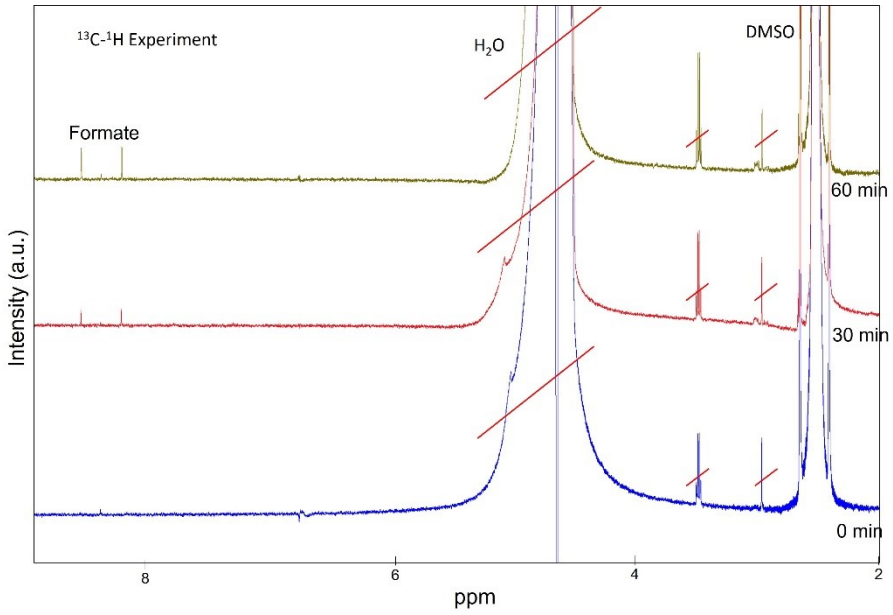

Figure S13. Stack plot of ^{13}C-^{1}H NMR experimental data for solution after electrocatalytic reduction of isotopically labeled $^{13}CO_2$ using 3-PTI/HCuCl at time intervals of 0 min, 30 min and 60 min. Growth of a doublet peak corresponding to ^{13}C-formate is labeled.

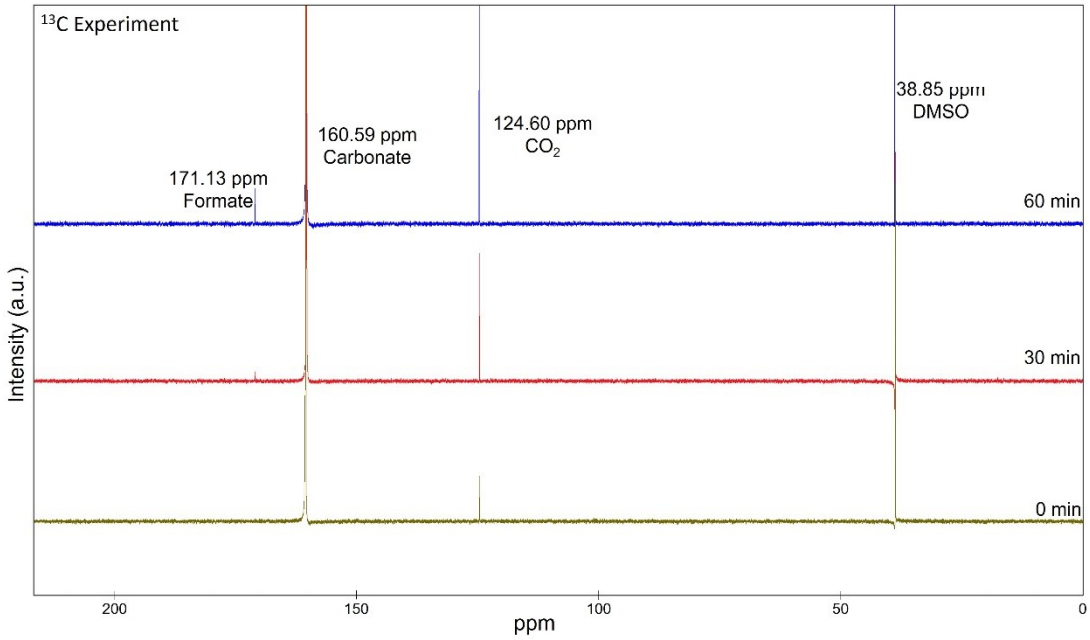

Figure S14. Stack plot of ^{13}C NMR experimental data for the solution after electrocatalytic reduction of isotopically labeled $^{13}CO_2$ using 3-PTI/HCuCl at time intervals of 0 min, 30 min and 60 min. Growth of the ^{13}C-formate peak is labeled.

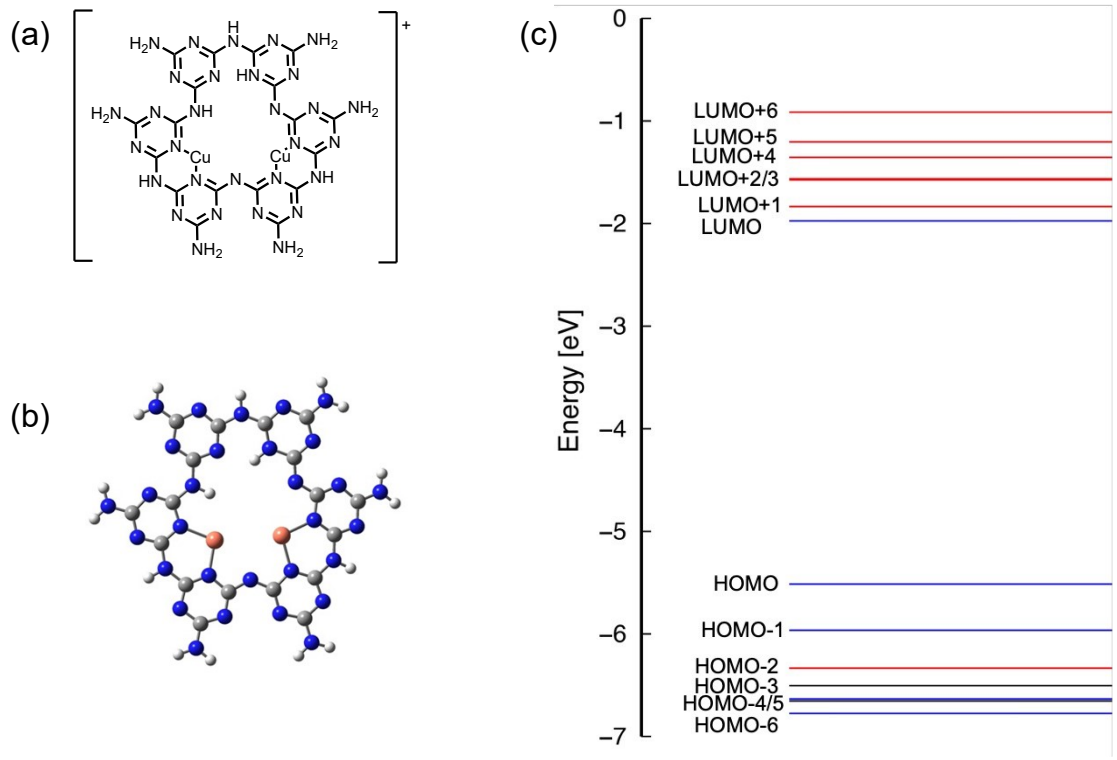

Figure S15. ChemDraw structure (a), geometry optimized structure (b) and calculated orbital energy level diagram (c) of starting PTI/Cu_2 complex. Blue lines represent metal-based orbital (Cu) and red lines represent ligand-based (PTI).

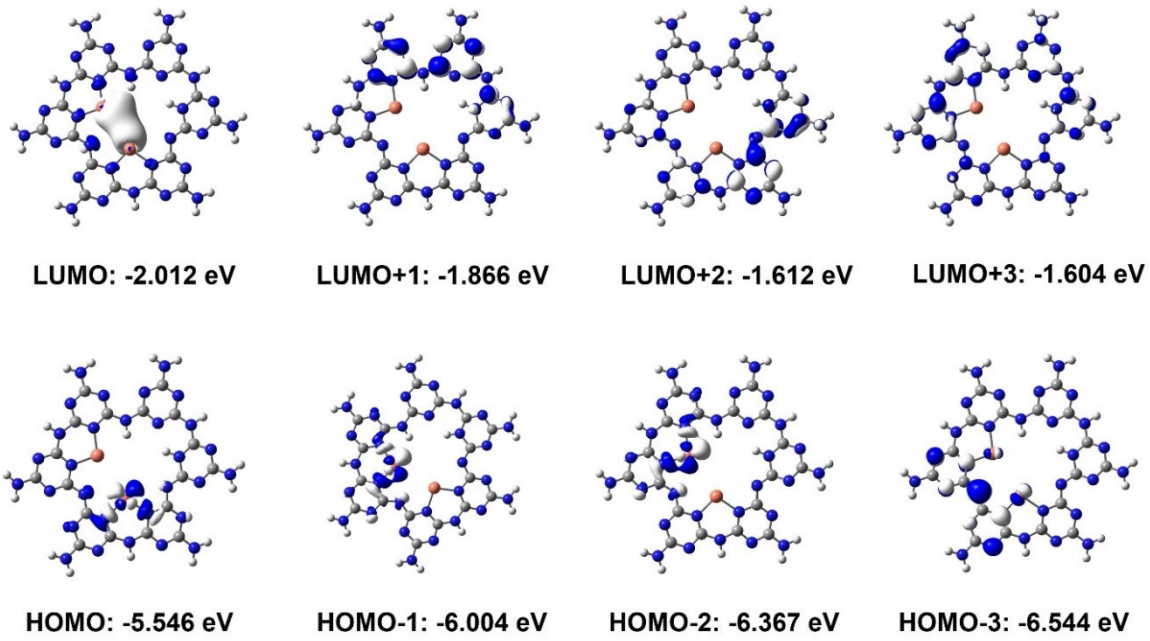

Figure S16. Calculated (starting) molecular orbitals for the frontier energy levels of an isolated section of the PTI/Cu-high structure containing the two Cu atoms within the intralayer cavity, prior to CO_2 coordination or electron reduction. Isosurface contours of electron density indicated by blue/white shading.

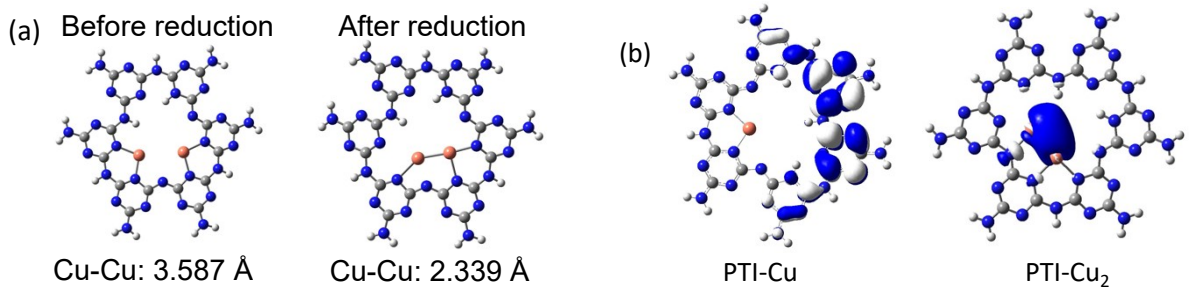

Figure S17. (a) Geometry optimized structures of PTI-Cu_2 before and after 1st electron reduction showing the Cu-Cu bond distances. (b) Natural Orbitals of PTI-Cu and PTI-Cu_2 with occupation numbers of 1.00.

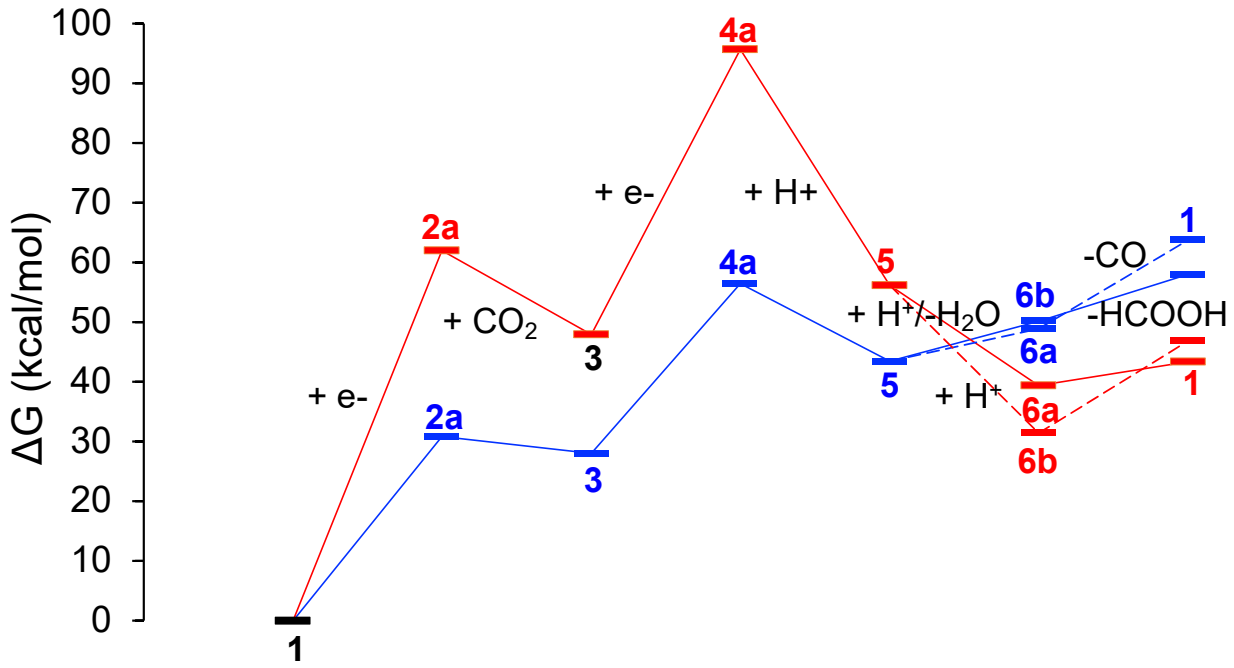

Figure S18. Calculated reaction coordinate diagram for CO_2 reduction within the Cu-atom pore of the PTI-Cu (in red) and PTI-Cu_2 (in blue), with labels to accompany the intermediates as illustrated in Figure 4.

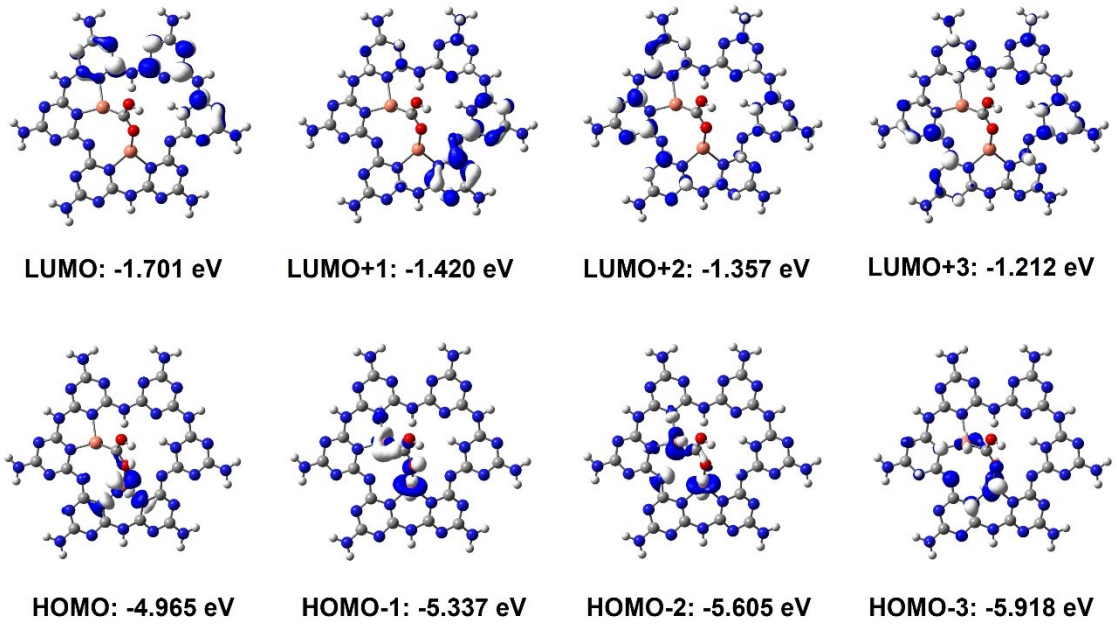

Figure S19. Calculated molecular orbitals for the frontier energy levels of intermediate 5, i.e., [PTI-Cu-COOH], which after protonation of the C or O atoms leads to the HCOOH or CO products, respectively. Isosurface contours of electron density indicated by blue/white shading.

Product Analysis Conducted at the CHASE SFPA Facility:

Gas chromatography equipment configuration. The identification and quantification of gaseous reaction products were performed with a custom-built Agilent 8890 Gas Chromatography equipment. The valve system and column configuration of the GC is illustrated in **Figure S19**. A Carbon Plot (column 1) and a Mol Sieves (column 2) column are installed in series through a switching valve. The Carbon Plot decelerate the elution of CO_2 relative to other gases such as O_2, N_2, H_2, and CO. The Mol Sieves column is used for separation of gaseous products with specific retention times. A Thermal Conductivity Detector is used to primarily monitor O_2, N_2, and H_2. A methanizer (nickel hydrogenation catalyst) is paired with a Flame Ionization Detector (FID) for enhanced sensitivity to detect CO_2, CH_4 and CO, which is done in series with the TCD measurements. Argon is used as the carrier gas. Details pertaining to method configuration are listed in **Tables S7-S10.**

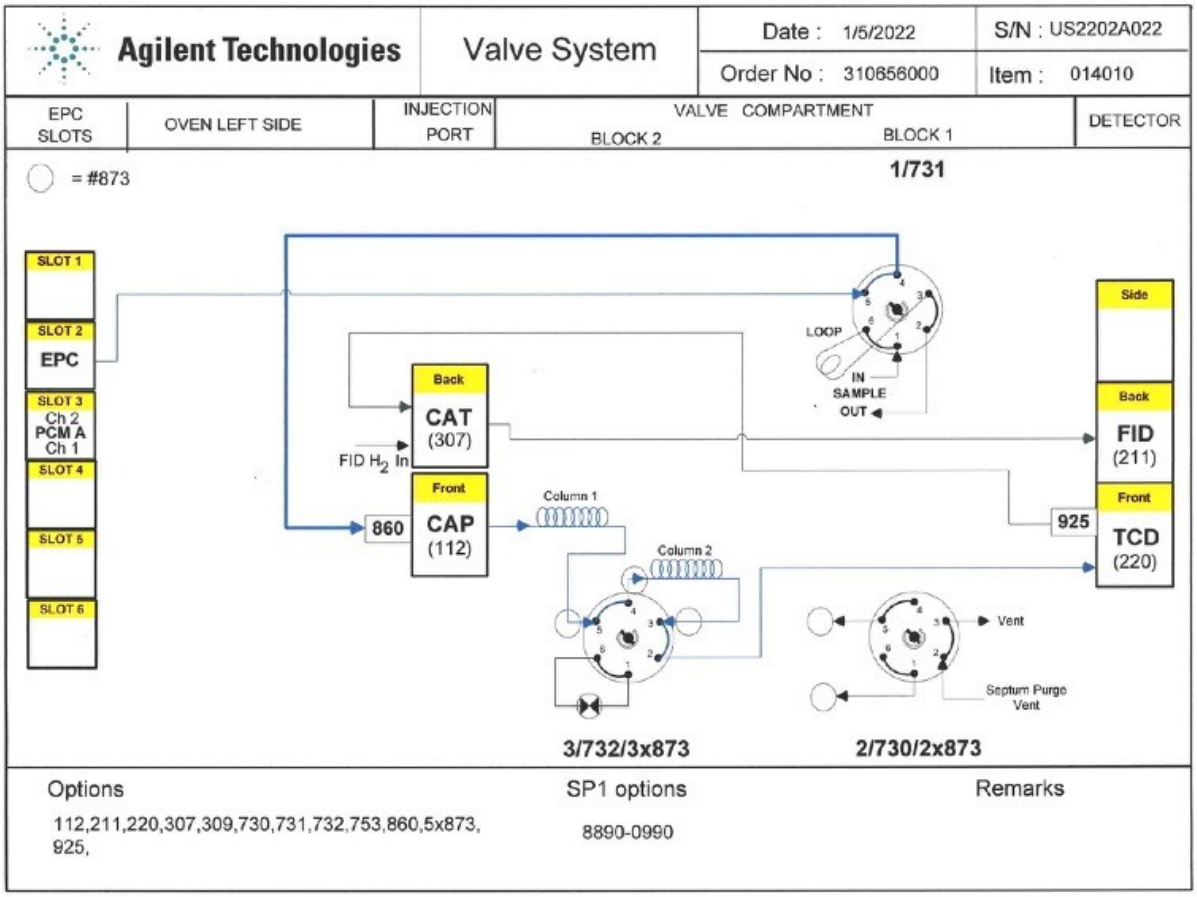

Figure S20. Valve system of the custom-built Agilent 8890 GC.

Table S7. GC Method configuration.

Carrier Gas	Argon	Grade: UHP
Makeup Gas	Nitrogen	Grade: UHP
Inlet Temperature	200 °C	
Inlet Pressure/Flow	28.393 psi	22 mL/min
Inlet Mode	Splitless	20 mL/min at 0.1 min
Columns	Carbon Plot Mol Sieves	(15 m, 0.32 mm, 1.5 µm) (30 m, 0.32 mm, 12 µm)
Column Pressure/Flow	28.707 psi	4 mL/min
Oven Temperature	40 °C	8 min
TCD Detector	250 °	Reference flow: 20 mL/min Makeup flow: 6 mL/min
FID Detector	250 °C	Air flow: 450 mL/min H_2 fuel flow: 5 mL/min Makeup flow: 45 mL/min
Auxiliary Heaters	Nickel Catalyst	375 °C

Table S8. Gas sampling valve events.

Valve	Event Type	Time (min)	Setpoint
Valve 1	Puts sample loop in line with injection inlet	0.01	ON
Valve 1	Equilibration before injection	1	OFF

Table S9. Switching valve events – for isolation of Mol sieves column and CO_2 bypass.

Valve	Event	Time (min)	Setpoint
Valve 3	Isolates mol sieves	1.4	ON
Valve 3	Connects mol sieves	1.8	OF

Table S10. Retention time of known gases.

Gas	H_2	O_2	N_2	CH_4	CO
Retention Time (min)	3.1	3.4	3.9	4.6	7.1

Sampling of the headspace. A sample loop of 100 µL with additional inlet/outlet tubing are connect to a gas sampling valve for automated inline sampling. The total volume of such *sampling line* is 126 µL. A vacuum pump is connected to the outlet of the sampling line and is used to build 126 µL of static vacuum. When the headspace of the reaction vessel (e.g. a photoelectrochemical cell) is opened to the evacuated sampling line, a sampling aliquot is brought into the GC for injection. Computer controlled solenoid-based isolation valves are used to control the sampling sequence, which can be done manually or automated.

Calibration curves of known gaseous products were prepared by titrating known volumes (µL) of the gas into a recipient of known volume (L) saturated with CO_2 as the gas matrix. Plots of the peak area associated with each gaseous product in the chromatogram, versus the gas titrated in units or parts per million (ppm) were used to calibrate the instrument response to a quantitative conversion factor (Cal_{CO} = 11.994 ppm/area ; Cal_{H2} = 199.884 ppm/area).

Quantification of gaseous products. Conversion of the amount of gaseous product in units of ppm to units of volume requires knowledge of the headspace volume (V_{hs}) during the experiment and the molar volume of the gas (*V/n*), according to **Equation 2**.

$$\frac{V}{n} = \frac{R\,T}{P} \tag{2}$$

Where *V* is the volume (L), *n* is the number of moles (mol), *R* is the gas constant (0.082 L atm mol^{-1} K^{-1}), *T* is temperature (K), and *P* is pressure (atm). For *n* = 1 mol, *T* = 298.15 K (room temperature), and *P* = 1 atm, the molar volume of a gas (*V*/*n*) is equal to 24.45 L/mol.

The general equation for quantifying gaseous products, in the gas phase, using the GC method and a calibration curve is given below.

$$Gas[mol] = \frac{\left(Gas[GC\ area]\ Cal\left[\frac{ppm}{area}\right]V_{hs}[L]\right) \times 10^{-6}}{0.082\left[\frac{L}{\quad}\right] \times T[K]} \tag{3}$$

Note that most calibration curves prepared by GC methods (like the one discussed above) do not include the amount of gas dissolved in the liquid phase, such as an electrolyte solution, during measurements. For the means of this work, the dissolved gaseous product were considered to be negligible, due to low solubility of H_2 and CO as well as having all FE values being calculated after 30 minutes or more of the potential hold, at which point dissolved gaseous products would have a more constant value.

References:

1) Pauly, M.; Kröger, J.; Duppel, V.; Murphey, C.; Cahoon, J.; Lotsch, B.V.; Maggard, P.A. “Unveiling the Complex Configurational Landscape of the Intralayer Cavities in a Crystalline Carbon Nitride” *Chem. Sci.* **2022**, *13*, 3187-3193.

2) Toby, B.H.; Vol Dreele, R.B.V. “GSAS-II: The Genesis of a Modern Open-Source All Purpose Crystallography Software Package” *J. Appl. Cryst.* **2013**, *46*, 544-549.

3) Wirnhier, E.; Döblinger, M.; Gunzelmann, D.; Senker, J.; Lotsch, B.V.; Schnick, W. “Poly(Triazine Imide) with Intercalation of Lithium and Chloride Ions $[(C_3N_3)_2(NH_2Li_{1-x})_3 \cdot LiCl]$: A Crystalline 2D Carbon Nitride Network” *Chem. Eur. J.* **2011**, *17*, 3213-3221.

4) Mesch, M.B.; Bärwinkel, K.; Krysiak, Y.; Martineau, C.; Taulelle, F.; Neder, R.B.; Kolb, U.; Senker, J. “Solving the Hydrogen and Lithium Substructure of Poly(Triazine Imide)/LiCl Using NMR Crystallography” *Chem. Eur. J.* **2016**, *22*, 16878-16890.

5) Suter, T.M.; Miller, T.S.; Cockcroft, J.K.; Aliev, A.E.; Wilding, M.C.; Sella, A.; Cora, F.; Howard, C.A.; McMillan, P.F. “Formation of Ion-Free Crystalline Carbon Nitride and its Reversible Intercalation with Ionic Species and Molecular Water” *Chem. Sci.* **2019**, *10*, 2519.

6) Wang, J.; Hao, D.; Ye, J.; Umezawa, N. “Determination of Crystal Structure of Graphitic Carbon Nitride: Ab Initio Evolutionary Search and Experimental Validation” *Chem. Mater.* **2017**, *29*, 2694–2707.

7) Hybertsen, M. S.; Louie, S. G. “First-Principles Theory of Quasiparticles: Calculation of Band Gaps in Semiconductors and Insulators” *Phys. Rev. Lett.* **1985**, *55*, 1418-1421.

8) Onida, G.; Reining, L.; Rubio, A. “Electronic Excitations: Density-Functional Versus Many-Body Green's-Gunction Approaches” *Rev. Mod. Phys.* **2002**, *74*, 601-659.

9) Paolo, G.; Stefano, B.; Nicola, B.; Matteo, C.; Roberto, C.; Carlo, C.; Davide, C.; Guido, L. C.; Matteo, C.; Ismaila, D.; Andrea Dal, C.; Stefano de, G.; Stefano, F.; Guido, F.; Ralph, G.; Uwe, G.; Christos, G.; Anton, K.; Michele, L.; Layla, M.-S.; Nicola, M.; Francesco, M.; Riccardo, M.; Stefano, P.; Alfredo, P.; Lorenzo, P.; Carlo, S.; Sandro, S.; Gabriele, S.; Ari, P. S.; Alexander, S.; Paolo, U.; Renata, M. W., “QUANTUM ESPRESSO: A Modular and Open-Source Software Project for Quantum Simulations of Materials” *J. Phys.: Conden. Matt.* **2009**, *21*, 395502.

10) Schlipf, M.; Gygi, F. “Optimization Algorithm for the Generation of ONCV Pseudopotentials” *Comput. Phys. Comm.* **2015**, *196*, 36-44.

11) Hamann, D. R. “Optimized Norm-Conserving Vanderbilt Pseudopotentials” *Phys. Rev. B* **2013**, *88*, 085117.

12) Perdew, J. P.; Ernzerhof, M.; Burke, K. “Rationale for Mixing Exact Exchange with Density Functional Approximations” *J. Chem. Phys.* **1996**, *105*, 9982-9985.

13) Carnimeo, I.; Baroni, S.; Giannozzi, P. “Fast Hybrid Density-Functional Computations Using Plane-Wave Basis Sets” *Electr. Struc.* **2019**, *1*, 015009.

14) Deslippe, J.; Samsonidze, G.; Strubbe, D. A.; Jain, M.; Cohen, M. L.; Louie, S. G., “BerkeleyGW: A Massively Parallel Computer Package for the Calculation of the Quasiparticle and Optical Properties of Materials and Nanostructures” *Comput. Phys. Comm.* **2012**, **183**, 1269-1289.

15) Monkhorst, H. J.; Pack, J. D. “Special Points for Brillouin-Zone Integrations” *Phys. Rev. B* **1976**, *13*, 5188-5192.

16) Becke, A. D. "Density-Functional Exchange-Energy Approximation with Correct Asymptotic Behavior" *Phys. Rev. A* **1988,** *38*, 3098.

17) Krishnan, R.; Binkley, J. S.; Seeger, R.; Pople, J. A. "Self-consistent molecular orbital methods. XX. A basis set for correlated wave functions" *J. Chem. Phys.* **1980,** *72*, 650-654.

18) McLean, A. D.; Chandler, G. S. "Contracted Gaussian Basis Sets for Molecular Calculations. I. Second Row Atoms, Z= 11–18" *J. Chem. Phys.* **1980,** *72*, 5639-5648.

19) Dolg, M.; Wedig, U.; Stoll, H.; Preuss, H. "Energy-Adjusted ab initio Pseudopotentials for the First Row Transition Elements" *J. Chem. Phys.* **1987,** *86*, 866-872.

20) Scalmani, G.; Frisch, M. J. "Continuous Surface Charge Polarizable Continuum Models of Solvation. I. General Formalism" *J. Chem. Phys.* **2010,** *132*, 114110.

21) Roy, L. E.; Jakubikova, E.; Guthrie, M. G.; Batista, E. R. "Calculation of One-Electron Redox Potentials Revisited. Is It Possible to Calculate Accurate Potentials with Density Functional Methods?" *J. Phys. Chem. A* **2009,** *113*, 6745-6750.

22) Frisch, M. J.; Trucks, G. W.; Schlegel, H. B.; Scuseria, G. E.; Robb, M. A.; Cheeseman, J. R.; Scalmani, G.; Barone, V.; Petersson, G. A.; Nakatsuji, H.; Li, X.; Caricato, M.; Marenich, A. V.; Bloino, J.; Janesko, B. G.; Gomperts, R.; Mennucci, B.; Hratchian, H. P.; Ortiz, J. V.; Izmaylov, A. F.; Sonnenberg, J. L.; Williams; Ding, F.; Lipparini, F.; Egidi, F.; Goings, J.; Peng, B.; Petrone, A.; Henderson, T.; Ranasinghe, D.; Zakrzewski, V. G.; Gao, J.; Rega, N.; Zheng, G.; Liang, W.; Hada, M.; Ehara, M.; Toyota, K.; Fukuda, R.; Hasegawa, J.; Ishida, M.; Nakajima, T.; Honda, Y.; Kitao, O.; Nakai, H.; Vreven, T.; Throssell, K.; Montgomery Jr., J. A.; Peralta, J. E.; Ogliaro, F.; Bearpark, M. J.; Heyd, J. J.; Brothers, E. N.; Kudin, K. N.; Staroverov, V. N.; Keith, T. A.; Kobayashi, R.; Normand, J.; Raghavachari, K.; Rendell, A. P.; Burant, J. C.; Iyengar, S. S.; Tomasi, J.; Cossi, M.; Millam, J. M.; Klene, M.; Adamo, C.; Cammi, R.; Ochterski, J. W.; Martin, R. L.; Morokuma, K.; Farkas, O.; Foresman, J. B.; Fox, D. J. *Gaussian 16 Rev. C.01*, Wallingford, CT, **2016**.

23) Liao, C. Z.; Lau, V. W. H.; Su, M.; Ma, S.; Liu, C.; Chang, C. K.; Sheu, H. S.; Zhang, J.; Shih, K. Unraveling the Structure of the Poly(Triazine Imide)/LiCl Photocatalyst: Cooperation of Facile Syntheses and a Low-Temperature Synchrotron Approach. *Inorg. Chem.* **2019**, *58* (23), 15880–15888. https://doi.org/10.1021/acs.inorgchem.9b02287.